Meteoritics & Planetary Science 41, Nr 2, 197–209 (2006)
Abstract available online at http://meteoritics.org

SIMS studies of Allende projectiles fired into Stardust-type aluminum foils at 6 km/sec

Peter HOPPE[1*], Frank J. STADERMANN[2], Thomas STEPHAN[3], Christine FLOSS[2], Jan LEITNER[3], Kuljeet K. MARHAS[1], and Friedrich HÖRZ[4]

[1]Max Planck Institute for Chemistry, Particle Chemistry Department, P.O. Box 3060, 55020 Mainz, Germany
[2]Laboratory for Space Sciences, Physics Department, Washington University, Saint Louis, Missouri 63130–4862, USA
[3]Institut für Planetologie, Universität Münster, Wilhelm-Klemm-Str. 10, 48149 Münster, Germany
[4]NASA Johnson Space Center, Houston, Texas 77058, USA
[*]Corresponding author. E-mail: hoppe@mpch-mainz.mpg.de

(Received 28 October 2005; revision accepted 4 February 2006)

Abstract–We have explored the feasibility of C, N, and O isotopic measurements by NanoSIMS and of elemental abundance determinations by time-of-flight secondary ion mass spectrometry (TOF-SIMS) on residues of Allende projectiles that impacted Stardust-type aluminum foils in the laboratory at 6 km/sec. These investigations are part of a consortium study aimed at providing the foundation for the characterization of matter associated with microcraters that were produced during the encounter of the Stardust space probe with comet 81P/Wild-2. Eleven experimental impact craters were studied by NanoSIMS and eighteen by TOF-SIMS. Crater sizes were between 3 and 190 μm. The NanoSIMS measurements have shown that the crater morphology has only a minor effect on spatial resolution and on instrumental mass fractionation. The achievable spatial resolution is always better than 200 nm, and C and O isotopic ratios can be measured with a precision of several percent at a scale of several 100 nm, which is the typical size of presolar grains. This clearly demonstrates that presolar matter, provided it survives the impact into the aluminum foil partly intact, is recognizable even if embedded in material of solar system origin. TOF-SIMS studies are restricted to materials from the crater rim. The element ratios of the major rock-forming elements in the Allende projectiles are well-characterized by the TOF-SIMS measurements, indicating that fractionation of those elements during impact can be expected to be negligible. This permits chemical information on the type of impactor material to be obtained. For any more detailed assignments to specific chondrite groups, however, information on the abundances of the light elements, especially C, is crucial. This information could not be obtained in the present study due to unavoidable contamination during impact experiments.

INTRODUCTION

Extraterrestrial matter exhibits characteristic fingerprints of elemental and isotopic compositions. At the macroscopic scale, isotopic anomalies are generally small (permil to percent level), but elemental and isotopic compositions of bulk samples can be used to differentiate between different types of meteorites. Rare but important constituents of primitive meteorites are the presolar dust grains that survived the events that led to the formation of the solar system (Hoppe and Zinner 2000; Zinner 2004). Presolar grains are characterized by large isotopic anomalies in their major elements (e.g., C and O) compared to materials that formed in the solar system, indicating that they formed around evolved stars (mainly red giants and supernovae). Presolar grains can be analyzed with high precision in the laboratory and have provided a wealth of astrophysical information. Presolar minerals identified to date include diamonds, silicon carbide (SiC), graphite, silicon nitride (Si_3N_4), corundum (Al_2O_3), spinel ($MgAl_2O_4$), hibonite ($CaAl_{12}O_{19}$), and various silicates. Recently, presolar grains were also found in interplanetary dust particles (IDPs) (e.g., Messenger et al. 2003; Floss et al. 2004; Stadermann and Floss 2004) and in Antarctic micrometeorites (Yada et al. 2005). In many IDPs, the abundances of presolar grains are higher than those in primitive meteorites, indicating the even more primitive nature of these particles (Messenger et al. 2003; Floss and Stadermann 2004). IDPs also exhibit widespread isotopic anomalies in H and N (enrichments in D and ^{15}N), often associated with organic matter, that are believed to be the

result of chemical reactions in the cold and dense molecular cloud from which our solar system formed (Messenger and Walker 1997).

Comets are assumed to represent the most primitive matter in our solar system. Our current understanding of the chemical and isotopic composition of comets is partly based on in situ studies, e.g., the flyby of comet 1P/Halley in 1986 (Jessberger et al. 1988; Jessberger and Kissel 1991), partly on spectral and other remote sensing studies of cometary coma. In contrast, the ongoing Stardust mission has collected cometary material during the flyby of comet 81P/Wild-2, as well as contemporary interstellar dust (Brownlee 2003; Tsou 2003); therefore, it is the first mission to return extraterrestrial rocky material from a specific solar system object other than the Moon. After the return of the cometary samples to Earth in January 2006, the primary goal is to determine the elemental, isotopic, mineralogical, and organic composition of the dust. Among the most important goals is the identification of presolar materials. Other objectives include the comparison of the cometary dust with other known extraterrestrial materials, such as primitive meteorites that formed early in the solar system. Such information can provide useful constraints on the history of Wild-2, for example, with respect to parent-body processing.

The Stardust mission will provide two different types of capture media containing cometary samples (Tsou 2003). The primary sampling material is low-density silica aerogel. In addition to the 1039 cm^2 surface area of exposed aerogel, composed of 132 individual cells, some 153 cm^2 of aluminum foil (Al 1100; >99% pure) was exposed. The primary purpose of this foil was to fix the aerogel in the modular collector trays and to facilitate the removal of individual tiles following return to Earth.

Although particles are not expected to survive unaltered at an encounter speed of 6.1 km/sec, the Al foil represents a valuable target material, especially for small (submicrometer) or loosely aggregated, fluffy particles that will disintegrate during penetration of the aerogel and therefore cannot be extracted with ease from this highly porous and friable capture medium. Isolated presolar grains or organic interstellar matter are expected to retain their isotopic signatures during impact and, even if they are embedded in matter of solar system origin, it is expected that their specific isotopic fingerprints, although likely to be diluted, can still be recognized. In addition, even totally vaporized projectiles can still be identified on the basis of thin-film vapor deposits that are accessible for SIMS analyses (Stadermann et al. 1994).

Here we report on NanoSIMS and time-of-flight secondary ion mass spectrometry (TOF-SIMS) analyses of crater residues on Al foils from impact experiments using material from the Allende CV3 meteorite. These shots were part of the dress rehearsal for Stardust. They were not performed specifically for the present study, but for the entire analytical community to practice with. The measurements were done with the Cameca NanoSIMS 50 ion microprobes at Washington University (Saint Louis, Missouri, USA) and at the Max Planck Institute for Chemistry (MPI) (Mainz, Germany) and with the ION-TOF TOF-SIMS IV instrument at the University of Münster (Münster, Germany). The NanoSIMS (Hillion et al. 1994), characterized by high spatial resolution and high sensitivity, has been successfully applied in various studies of presolar materials (e.g., Floss et al. 2004; Hoppe and Besmehn 2002; Messenger et al. 2003; Mostefaoui and Hoppe 2004; Nguyen and Zinner 2004; Stadermann et al. 2005). The TOF-SIMS technique has been used for the analysis of extraterrestrial matter for more than a decade (Stephan 2001), including the analysis of impact residues from the Long Duration Exposure Facility (LDEF) (Stephan et al. 1992) and the Hubble Space Telescope solar array (Stephan et al. 1995).

Conventional SIMS has been used in the past to measure the isotopic compositions of a large number of elements in situ at a scale of several micrometers (Zinner 1989). The NanoSIMS permits isotopic analyses to be done even at the submicrometer scale with sufficiently high precision to identify presolar materials. For example, the O isotopic compositions of 500 nm-sized spinel grains can be measured with a precision of several percent (Zinner et al. 2005) with analysis times of only a few minutes. The TOF-SIMS technique is particularly useful if elemental compositions of thin layers are to be measured. Due to its high sensitivity, useful elemental information can be obtained from only a few monolayers of material with a lateral resolution at the submicrometer scale. Detection limits are typically <1 ppm. These features provide significant advantages over other elemental mapping techniques, such as energy dispersive X-ray (EDX) measurements. For the latter, detection limits vary with element (e.g., ~0.1% for Fe and ~1% for Mg and Si) and the information depth depends on the electron energy and varies between several 100 nm for 5 keV electrons (only the light to intermediate-mass elements can be detected) to >1 μm for 20 keV electrons. In the experimental setup considered here, EDX typically delivers a greater share of the signal from the underlying Al foil than TOF-SIMS.

In anticipation of the Stardust samples, the major goals of this study were to answer the following questions: Are isotopic measurements of crater residues feasible by NanoSIMS? What is the achievable lateral resolution and what is the precision for the measurement of the isotopic compositions (C, N, O) of objects with the typical size (200 nm to >1 μm) of presolar grains? How well can the chemical composition of Allende be reproduced by the analysis with TOF-SIMS?

EXPERIMENTAL

Powdered bulk material of the CV3 chondrite Allende with a nominal size range of 38–43 μm was shotgunned into Al foils at a velocity of 5.9–6.1 km/sec using a 5 mm caliber light gas gun at NASA Johnson Space Center. The foils used

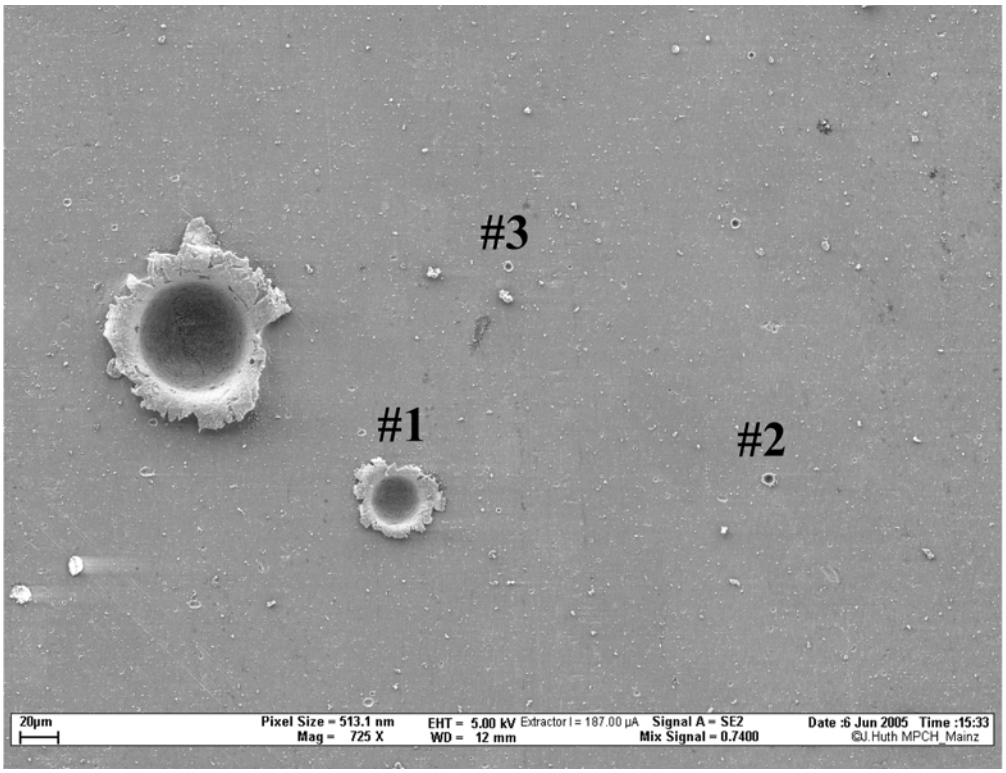

Fig. 1. SEM images of three craters (MPI #1/2/3) analyzed with the NanoSIMS. Crater sizes are 16, 5, and 3 μm, respectively.

are flight spares from Stardust, kindly provided by Dr. P. Tsou of the Jet Propulsion Laboratory; they are >99% pure (Al 1100 series) and 100 μm thick, and they draped a massive Al back plate, akin to the foils exposed on Stardust. Earlier studies had shown that projectiles of this size are expected to produce craters as large as 180 μm (Hörz et al. 1995; see also Kearsley et al. 2006). Due to the modestly coherent nature of the Allende meteorite, substantial fragmentation of the projectiles occurs during light-gas-gun acceleration (>10^6 *g*) and a wide range of fragment-associated crater sizes resulted in the present experiments. Actual projectiles responsible for many very small craters may thus be compositionally and mineralogically variable, ranging from, e.g., pure Allende matrix to monomineralic grains. Most craters are produced by Allende projectiles, yet some craters may also be due to unavoidable gun debris, such as abrasion products of the gun barrel or debris from the burst high pressure diaphragm. Typically, on a square target some 2 cm on a side, tens of craters are produced in a single experiment. Their diameters are between <1 and 200 μm, with most craters measuring <2 μm. For the SIMS studies, we concentrated on the larger craters with sizes between 3 and 190 μm.

Scanning electron microscopy (Leo 1530 FESEM at MPI and JEOL 840A SEM at Washington University) and optical scanning (at the University of Münster) were used to investigate the crater distribution and crater sizes on the Al foils (Figs. 1 and 2). A total of 29 craters on several Al foil pieces were selected for the SIMS analyses: NanoSIMS measurements were performed on 4 craters, 15 to 30 μm in size, at Washington University and on 7 craters (4 of which were located on an Al foil piece that was flattened prior to analysis), 3 to 30 μm in size, at MPI. The flattening was achieved by pressing the Al foil between two stainless steel plates. TOF-SIMS analyses were made on 18 craters, 4 to 190 μm in size, at the University of Münster. The detailed measurement scheme is given in Table 1.

The NanoSIMS measurements followed procedures previously applied in the study of extraterrestrial materials (Floss and Stadermann 2004; Mostefaoui and Hoppe 2004). Measurements were made with a Cs^+ primary beam and parallel detection of negative secondary ions of [^{16}O, ^{17}O, ^{18}O, ^{28}Si, $^{27}Al^{16}O$] and [^{12}C, ^{13}C, $^{12}C^{14}N$, $^{12}C^{15}N$, ^{28}Si] at MPI for Chemistry, and of [^{12}C, ^{13}C, ^{16}O, ^{17}O, ^{18}O] at Washington University. Prior to analysis, Cs was implanted for several minutes with a comparatively high primary current (~20 pA) into the region of interest to remove surface contamination and to get stable secondary ion yields. For the analysis, a primary Cs^+ ion beam of <1 pA was focused into a spot of <100 nm and raster ion images (256 × 256 to 1024 × 1024 pixels) of variable size (depending on crater diameter) were recorded for the selected craters. Images consist of up to 40 consecutive scans (layers) with total analysis times up to several hours per image. The measurement of isotopic standards was not necessary, since the primary goal was to investigate the effects of crater topography on secondary ion signal intensity, lateral

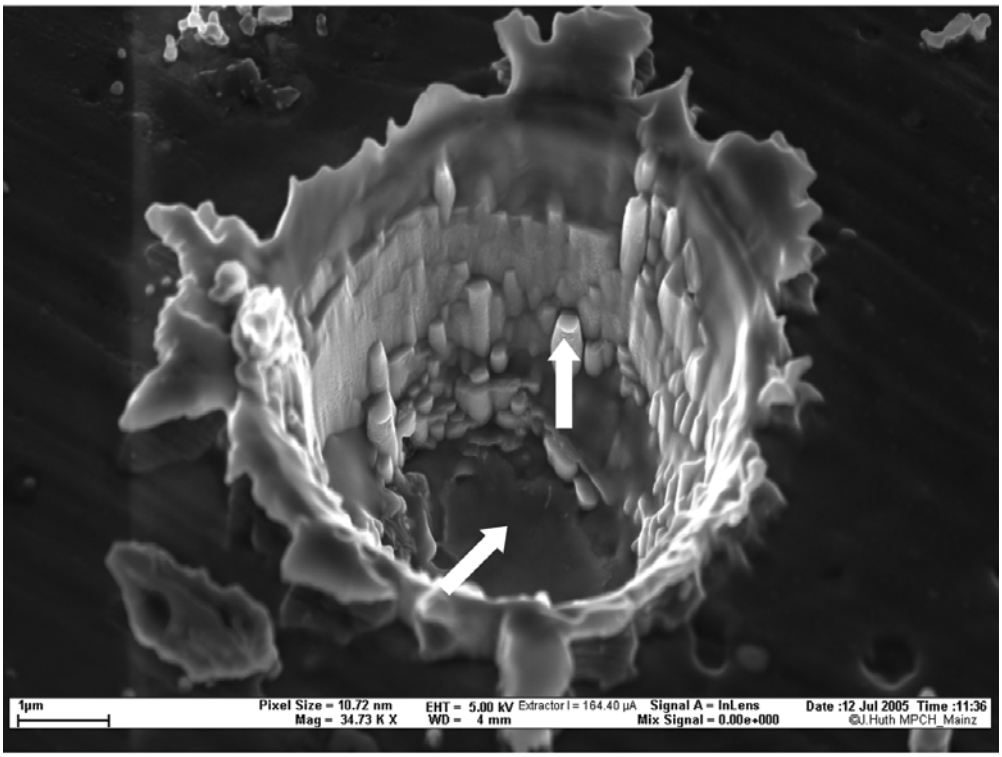

Fig. 2. An SEM image of crater MPI #2 after the NanoSIMS measurements. The sample is tilted by 30 degrees relative to the electron detector. The contrast in the image is mainly due to topographic features and the angle between sample and detector. Residues of the Allende projectiles can still be recognized along the wall (on top of the columns) and at the bottom of the crater (two examples are indicated by arrows; cf. Figs. 6 and 9).

resolution, and instrumental mass fractionation for C, N, and O isotopic measurements.

TOF-SIMS allows a comprehensive elemental analysis with relatively high lateral resolution and minute sample consumption (Stephan 2003). During a typical analysis, less than one atomic monolayer is consumed while the sample is rastered with a ~0.2 µm-sized Ga^+ primary ion beam. All secondary ions of a single polarity are detected quasi simultaneously after their passage through the time-of-flight spectrometer. Both polarities are measured in two consecutive analyses, each lasting typically up to twelve hours. Elemental, isotopic, and molecular compositions are determined in parallel. Further details on the TOF-SIMS technique are given in the literature (Stephan 2001). In the present study, all sample regions selected for TOF-SIMS analysis were measured after sputter cleaning by Ar ion bombardment. This cleaning was necessary since the entire Al foil was covered with a thin layer of mainly organic contaminants from the vaporized, polyethylene projectile sabot. Based on the distributions of Mg, Si, Ca, and Fe, regions of interest were selected from which complete mass spectra were generated. Mass spectra obtained from foil areas outside the craters were used for blank correction. For this blank correction, Al/Si-ratios of the projectile material were assumed to be CV-chondritic. The surplus in Al was attributed to the target blank. Uncertainties in blank corrections caused by variations of element ratios among different areas outside the craters yield the main contribution to the statistical errors of quantitative TOF-SIMS results in this study. Bulk element ratios were calculated using relative sensitivity factors obtained from glass standards that are usually used for quantitative TOF-SIMS analysis of silicates (Stephan 2001). These sensitivity factors, although obtained from ideally flat standards, have been successfully applied to uneven samples like whole IDPs (Rost et al. 1999). In addition, TOF-SIMS analysis of fracture surfaces of ALH 84001 (Stephan et al. 2003) did not reveal any detectable change in element ratios due to sample topography. Sample geometry is less critical in this respect for TOF-SIMS analyses than it is for NanoSIMS measurements. Also, other than the NanoSIMS studies, the TOF-SIMS data recorded here are not for the full crater depths. Therefore, possible effects of sample topography to element ratios for the crater residues are considered to be negligible.

RESULTS AND DISCUSSION

NanoSIMS Studies

The unflattened craters were investigated to determine the feasibility of direct NanoSIMS analysis of these geometrically complex structures. Crater depths are roughly half the crater diameter (Leroux et al. 2006). Since the

Table 1. Craters in Al foils produced by Allende projectiles at some 6 km/sec selected for NanoSIMS and TOF-SIMS studies.

Crater	Size (μm)	Foil preparation	Measurement	Method
WU #1	20		C, O	WU NanoSIMS
WU #2	15		C, O	**
WU #3	30		C, O	**
WU #4	20		C, O	**
MPI #1	26		C, N, O	MPI NanoSIMS
MPI #2	5		C, N, O	**
MPI #3	3		O	**
MPI #4	30	Flattening	C, N, O	**
MPI #5	13	Flattening	C, N, O	**
MPI #6	9	Flattening	O	**
MPI #7	9	Flattening	O	**
UM #1	120		Ion images + mass spectra	TOF-SIMS
UM #1.1	7		Ion images + mass spectra	**
UM #1.2	9 × 5		Ion images + mass spectra	**
UM #2	100		Ion images + mass spectra	**
UM #3	40		Ion images + mass spectra	**
UM #4	18		Ion images + mass spectra	**
UM #4.1	4		Ion images + mass spectra	**
UM #5	190		Ion images + mass spectra	**
UM #6	95		Ion images + mass spectra	**
UM #7	95		Ion images + mass spectra	**
UM #7.1	19		Ion images + mass spectra	**
UM #8	80		Ion images + mass spectra	**
UM #8.1	40		Ion images + mass spectra	**
UM #9	140		Ion images + mass spectra	**
UM #9.1	35		Ion images + mass spectra	**
UM #10	120		Ion images + mass spectra	**
UM #11	170		Ion images + mass spectra	**
UM #12	100		Ion images + mass spectra	**

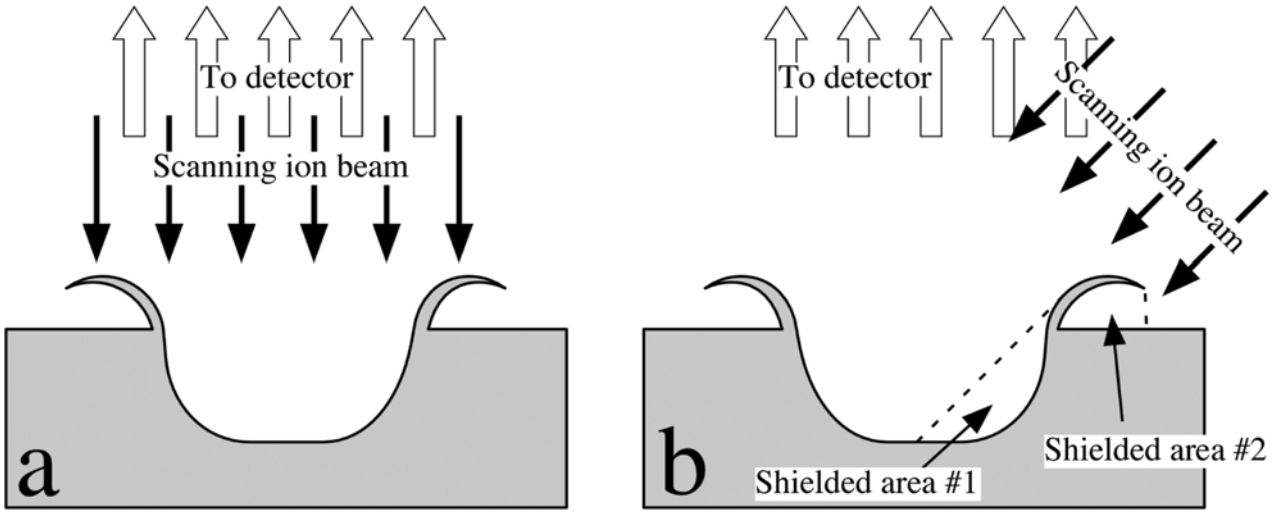

Fig. 3. The ion optics of the NanoSIMS (a) are designed in such a way that both incoming primary ion beam and secondary ion extraction are normal to the sample surface. This has advantages in the analysis of (unflattened) impact craters, because the entire crater bottom is visible in most craters without direct shading from the crater walls. In contrast to this, TOF-SIMS (b) cannot analyze major parts of the crater bottom, since primary ions reach the sample surface at an angle of 45°. Therefore, shielded area #1 is not reached by the primary ion beam. In addition, secondary ions from shielded area #2 cannot reach the detector. The latter effect causes the "shadow" on the outside of the craters in TOF-SIMS secondary ion images (cf. Fig. 11).

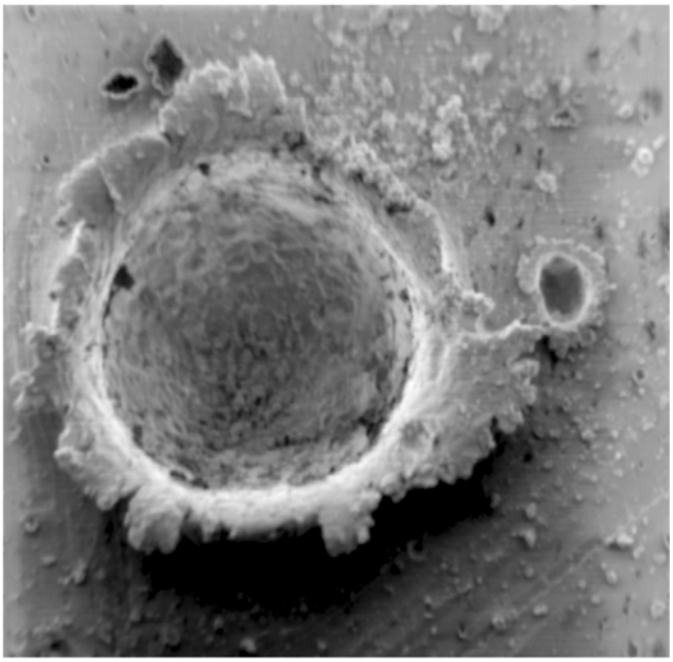

Fig. 4. Aluminum foil impact as seen by NanoSIMS secondary electron (SE) imaging. The diameter of the large crater (WU #1) is 20 μm; a smaller impact crater can be seen to the right. Since secondary electrons are extracted in parallel with the secondary ions, the spatial resolution and the field of view are identical in electron and ion images, although the signal intensity is in most cases lower for secondary ions.

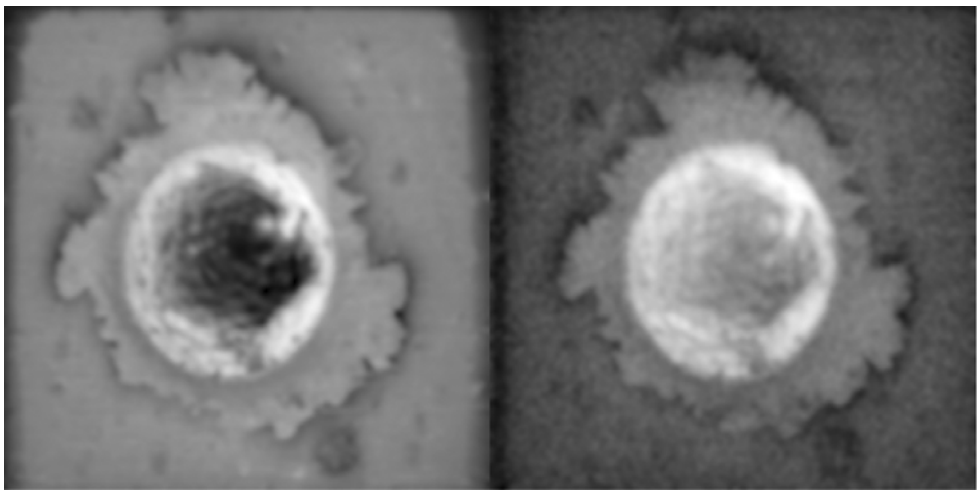

Fig. 5. Two NanoSIMS images of the secondary $^{16}O^-$ signal from the same impact crater (15 μm; WU #2). The efficiency of the secondary ion extraction is sample height dependent. In the image on the left the ion extraction is optimized for the surface of the Al foil. On the right, the instrument is optimized for the extraction of secondary ions from the significantly deeper crater bottom.

NanoSIMS has coaxial primary and secondary ion beams that are normal to the sample surface (Fig. 3a), it should be possible to image the entire crater without direct shading from the walls. This assumption turned out to be correct (Fig. 4), although the signal intensity was in some cases significantly reduced for ions extracted from the crater bottom. The apparent reduction turned out to be the result of a secondary ion beam alignment, which was optimized for the extraction of secondary ions from the exact height of the surrounding Al foil reference level (Fig. 5). By changing the secondary ion beam focusing plane, it was in many cases possible to increase the yield of secondary ions from the crater bottom. Practically, this was achieved by changing the settings for the EOS and L4 lenses as well as making adjustments to deflectors Cy, P2, and P3.

The surface of the Al foil shows significant contamination with a variety of elements, which interferes with an elemental or isotopic characterization of the debris material. Brief sputter cleaning with the primary beam in the SIMS instrument, however, was in most cases sufficient to

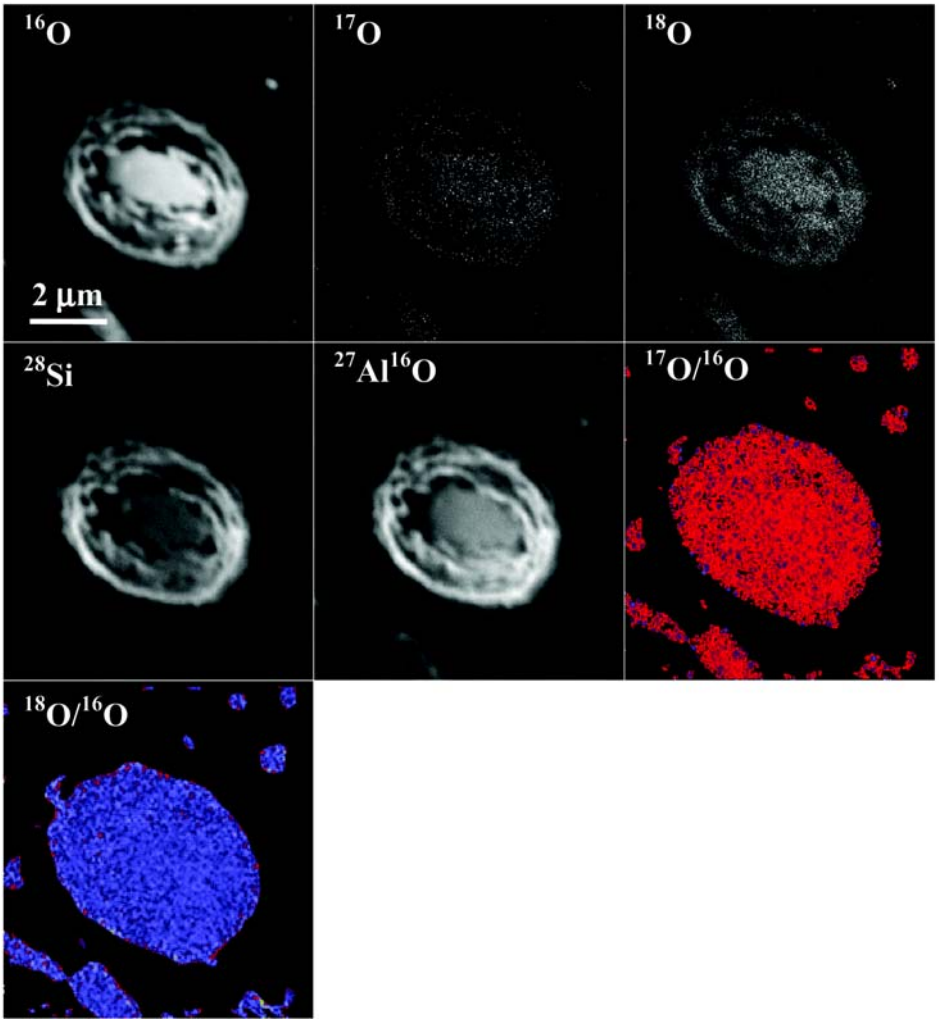

Fig. 6. NanoSIMS ion images (256 × 256 pixel) of $^{16}O^-$, $^{17}O^-$, $^{18}O^-$, $^{28}Si^-$, and $^{27}Al^{16}O^-$ and false-color $^{17}O/^{16}O$ and $^{18}O/^{16}O$ ratio images of crater MPI #2. The ratio images are masked, i.e., data are only shown for those regions that have a ^{16}O intensity that exceeds 10% of the pixel with the highest ^{16}O intensity. Standard deviations are 13% for $^{17}O/^{16}O$ and 5.4% for $^{18}O/^{16}O$ ratios in 12 × 12 pixel sub-areas (380 nm square). Most of the crater is covered by Allende material (cf. Fig. 2); differences in secondary ion intensities reflect crater topography (different relative effects for different elements) and also heterogeneities in the material distribution. Because ion emission is normal to the sample surface, the column structure seen in the tilted electron image (Fig. 2) is not seen in the ion images.

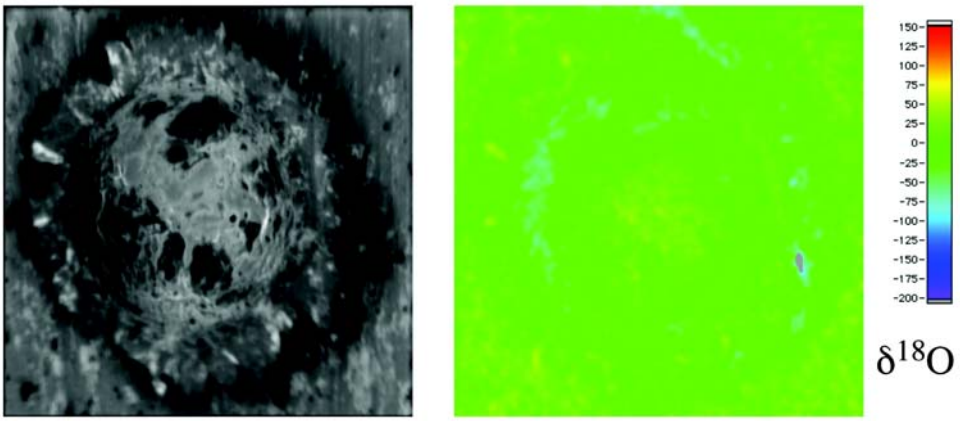

Fig. 7. NanoSIMS secondary $^{16}O^-$ signal (left) and false-color ^{18}O images (right) of an Al foil impact crater (WU #3) of 30 μm in size. Although the signal intensity varies greatly and the sample exhibits significant morphological variations, this has only a minor effect on the determination of the O isotopic ratios which vary by no more than 10% inside the crater.

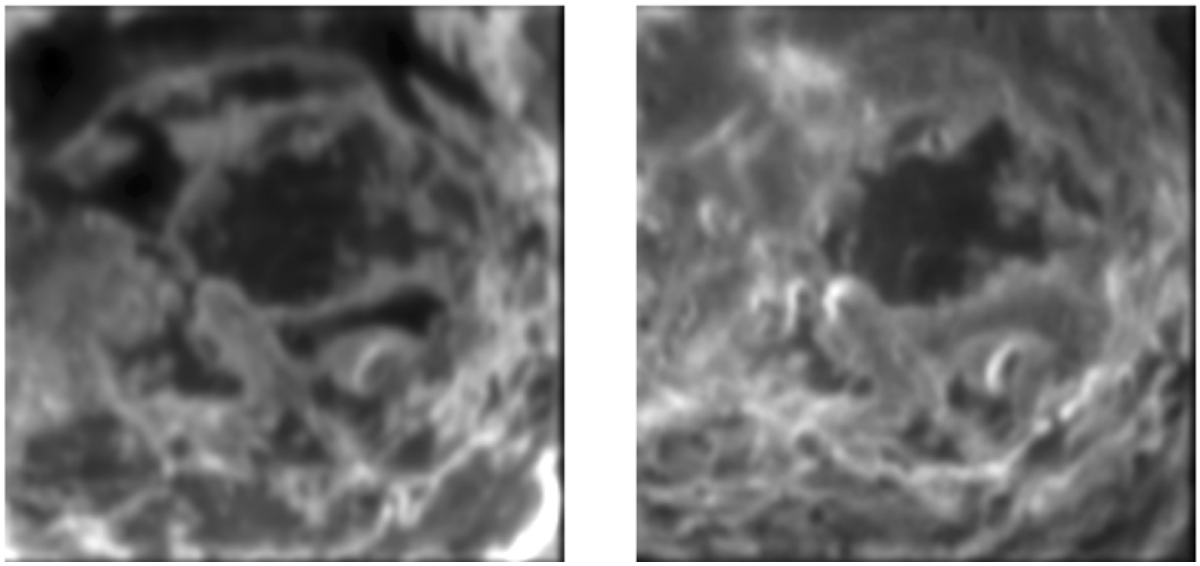

Fig. 8. NanoSIMS secondary electron (SE, left) and $^{28}Si^-$ secondary ion (right) images; 10 × 10 μm^2 detail of the crater bottom from Fig. 7. These images demonstrate that submicrometer details can easily be identified in the layer of impact debris at the crater bottom.

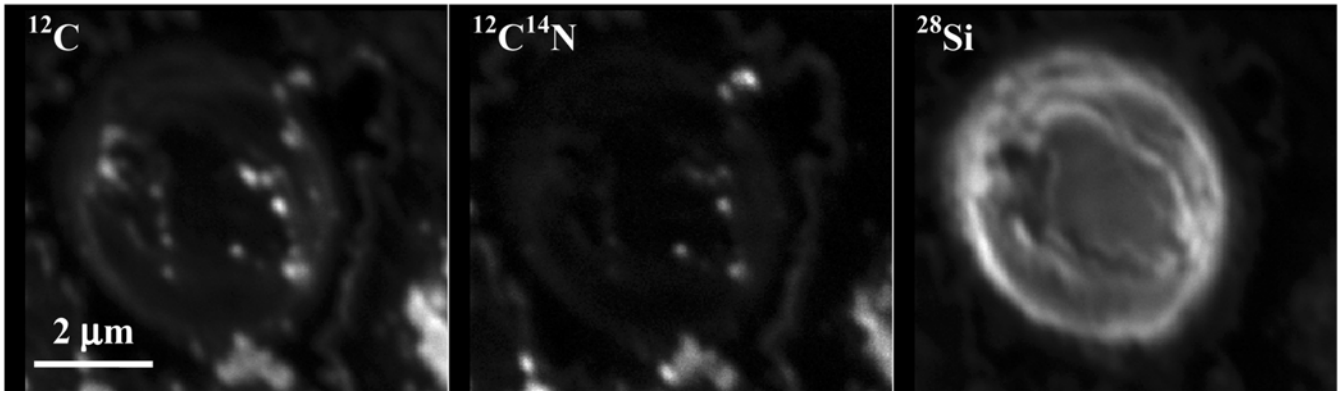

Fig. 9. NanoSIMS ion images (256 × 256 pixel) of $^{12}C^-$, $^{12}C^{14}N^-$, and $^{28}Si^-$ of crater MPI #2 (cf. Fig. 2). Other than O, Si, and Al, which are present almost everywhere inside the crater (Fig. 6), C and N are seen only in "hot spots" inside (150–500 nm in size) and outside the crater, possibly a hint for contamination.

remove the ubiquitous surface contamination layer. The remaining material on the surface of the Al foil is most likely residue from the impactor. The lateral resolution of the secondary ion images is important since a large fraction of previously identified presolar phases is in the submicrometer size range. Under ideal conditions, with a flat sample, the NanoSIMS can routinely resolve details as small as 50–100 nm. The lateral resolution in the crater bottom is somewhat reduced due to the distortion of the electrical extraction fields. However, several tests show (Figs. 6–10) that a spatial resolution on the order of 100–200 nm can be achieved even under less than ideal conditions. In completely flattened crater samples, the standard lateral resolution of 50–100 nm can be achieved.

The main purpose of the NanoSIMS measurements in the initial stage of the Stardust analyses will be the isotopic characterization of impact debris associated with microcraters. It is thus important to know to what extent the determination of isotopic ratios is affected by the extreme morphology of such craters. Si- and O-rich (Allende) material was found in all analyzed craters. Examples are shown in Figs. 5–9. Several tests clearly demonstrated (Figs. 6 and 7) that edge, slope, and sample height variations only have a minor effect on the measured isotopic ratios. For selected craters, we divided the crater area into sub-areas and calculated the $^{17}O/^{16}O$ and $^{18}O/^{16}O$ ratios in all sub-areas. The standard deviations of this data set can then be used to quantify relative variations in instrumental mass fractionation across the craters and the limitations imposed by counting statistics. This is to test whether isotopic heterogeneities would be recognizable, should presolar grains, assumed to be embedded in material of solar system origin, survive the foil

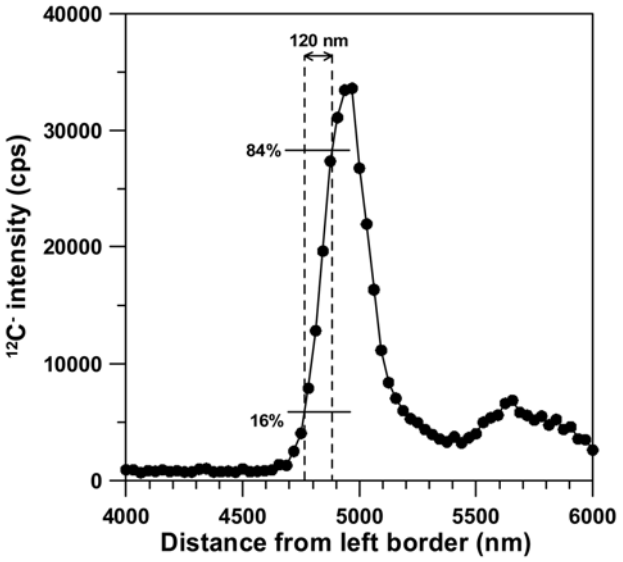

Fig. 10. Linescan for $^{12}C^-$ intensity through crater MPI#2 (cf. Fig. 9). An upper limit for the spatial resolution in the ion images can be calculated from the distance between the 16% and 84% intensity levels of the maximum signal of isolated particles. In this example, the spatial resolution is better than 120 nm.

impact partly intact. For sub-areas with sizes between 300 and 1200 nm (depending on crater size), we obtain standard deviations of 8–16% for $^{17}O/^{16}O$ and 5–10% for $^{18}O/^{16}O$, clearly sufficient to recognize presolar grains. These values are somewhat larger than expected from counting statistics, attesting to the fact that instrumental mass fractionation varies at the percent level across the crater. No significant difference was observed between flattened and unflattened craters. This probably reflects the fact that craters in flattened foils still exhibit topographic features. In addition, matrix effects may be partly responsible for the small variations in instrumental mass fractionation. Bulk $^{17}O/^{16}O$ and $^{18}O/^{16}O$ ratios (i.e., from the integrated O signal across the whole crater) between different craters on the same Al foil were found to differ typically by 1–2%. Since O isotopic compositions in presolar grains typically vary by a factor of 2 and sometimes even more (Messenger et al. 2003; Mostefaoui and Hoppe 2004; Nguyen and Zinner 2004; Nittler et al. 1997; Zinner et al. 2005), it will be possible to identify presolar materials among the debris particles.

C-rich grains were found in the majority of analyzed craters. One example is shown in Fig. 9. The mineralogy of the C-rich particles could not be determined. Whether they are from Allende or actual contamination is difficult to discern, but contamination seems to be more plausible, because C is also seen outside the craters (Fig. 9). In addition, a smaller amount of C is dispersed over the whole crater. The calculated standard deviations of $^{12}C/^{13}C$ and $^{15}N/^{14}N$ ratios of the C-rich particles (150–500 nm) in Fig. 9 are 5% and 26%, respectively. At least for C, this would be sufficient to identify carbonaceous presolar grains as most of these grains have isotopic anomalies of more than several ten percent (e.g., Hoppe and Zinner 2000; Zinner 2004).

Our NanoSIMS studies were performed on craters with sizes between 3 and 30 μm. However, we are confident that craters in a much larger size range from submicrometers to more than 100 μm can be studied.

TOF-SIMS studies

In contrast to the NanoSIMS, the primary ions in TOF-SIMS reach the sample surface at an angle of 45° (Fig. 3b). Therefore, major areas of the crater bottom are not accessible by the primary ion beam. As an example, Fig. 11 shows lateral element distributions in the area of craters UM #4 and UM #4.1. Secondary ion intensities on the right hand side of the crater rim are always highest since the primary ions reach the sample from the right, and ion yields increase when the incident beam becomes more oblique. The crater wall on the left hand side is hit almost perpendicularly, reducing the respective ion yields.

Another complication arises from the time-of-flight principle. Secondary ions from the crater bottom reach the detector slightly later than secondary ions of the same species that are released from the crater rim. Since the time scale is converted to a mass scale in TOF-SIMS, this delay can lead to undesirable mass interferences: elemental ions (typically at the low mass edge of a given nominal mass) from the crater bottom interfere with heavier molecular ions of the same nominal mass from the crater rim. In most cases, therefore, only secondary ions from the crater rim were used to calculate element ratios. Their identification in the mass spectra was always unambiguous.

Crater UM #1 does not provide any residual material for a proper impactor characterization. However, all other sample regions contain enough material for quantitative analysis. Quantitative results for all samples are summarized in Table 2 and Fig. 12; the element ratios normalized to Si show huge variations, especially for small craters. Deposit UM #1.2 and crater UM #5 exhibit extremely large depletions of more than a factor of ten in practically all rock-forming elements compared to CV chondritic ratios. These samples are probably contamination from gun debris and consequently were omitted from the calculation of geometric mean values shown in Fig. 12. Some other crater residues, although not showing the full range of elements characteristic of bulk chondrites, are consistent with the composition of individual constituents of CV3 chondrites, and were therefore included in the mean values since they might reflect heterogeneities in Allende material. The geometric mean values are close to CV element ratios for most elements and fit well within the range defined by Allende chondrules (Rubin and Wasson 1987).

Since sputter cleaning was necessary prior to TOF-SIMS analysis, no useful information on organic constituents of the projectiles could be obtained. Organic compounds usually fragment during Ar bombardment. Typical silicone oil

Table 2. Atomic element ratios relative to Si calculated from TOF-SIMS spectra for crater residues and normalized to CV chondrites (CV column according to Lodders and Fegley 1998).

	CV	#1.1	#1.2	#2	#3	#4	#4.1	#5	#6
Na	0.0265	<4.2	1.42(9)	1.5(8)	0.7(7)	0.33(7)	0.6(1)	2.416(6)	2.5(4)
Mg	1.05	1.8(1)	<0.012	1.2(1)	1.3(1)	0.522(6)	0.161(9)	0.0289(4)	1.05(3)
Si	1	1.0(7)	1.00(4)	1.0(2)	1.0(3)	1.00(3)	1.00(5)	1.000(3)	1.0(2)
K	0.00165	<8.9	0.8(2)	2(1)	2(2)	0.5(2)	1.3(3)	0.09(1)	1(1)
Ca	0.0821	0.7(1)	0.028(7)	5.7(2)	4.22(7)	0.051(5)	2.55(4)	0.272(1)	1.13(3)
Sc	0.000041	<6.7	<0.21	2(1)	1.5(9)	0.3(2)	<9.9	0.02(2)	2(1)
Ti	0.00325	<0.53	0.09(1)	1.1(5)	2.4(4)	0.15(2)	0.5(3)	0.08(2)	0.8(1)
V	0.000341	<0.67	<0.070	0.6(4)	0.8(4)	0.06(5)	<1.4	0.014(5)	0.8(3)
Cr	0.0120	1.1(1)	0.046(6)	0.66(5)	1.16(6)	0.37(1)	0.05(3)	0.0121(9)	0.31(3)
Mn	0.00495	0.9(4)	0.23(3)	0.6(1)	0.9(2)	0.66(3)	0.3(1)	0.019(2)	0.7(1)
Fe	0.753	0.84(8)	0.054(6)	0.42(6)	0.42(4)	0.413(5)	0.071(8)	0.0089(3)	0.42(2)
Co	0.00194	0.8(4)	0.02(1)	0.4(1)	0.7(2)	0.16(4)	<0.81	0.007(3)	0.4(1)
Ni	0.0402	0.4(2)	0.020(8)	0.23(6)	0.35(7)	0.13(2)	<0.082	0.013(2)	0.68(8)
	#7	#7.1	#8	#8.1	#9	#9.1	#10	#11	#12
Na	0.8(4)	1.0(4)	0.6(4)	2.6(3)	1.4(5)	0.5(1)	0.4(3)	13(1)	0.7(4)
Mg	0.90(3)	0.10(3)	1.25(3)	0.96(2)	0.92(4)	0.186(9)	1.20(2)	1.87(9)	1.11(3)
Si	1.0(2)	1.0(2)	1.0(2)	1.0(1)	1.0(2)	1.00(5)	1.0(1)	1.0(5)	1.0(2)
K	<2.4	2.6(9)	<2.2	3.5(7)	<3.2	0.5(3)	<1.8	4(3)	<2.9
Ca	2.15(3)	3.97(4)	0.49(3)	1.10(3)	1.59(4)	1.96(2)	0.77(2)	3.38(9)	1.43(3)
Sc	1.7(9)	<2.2	<2.0	<3.9	3(1)	4.7(2.4)	3(1)	5(2)	2.5(7)
Ti	0.9(2)	<0.84	0.36(9)	0.4(1)	0.8(2)	1.0(2)	0.59(9)	1.0(3)	0.8(1)
V	<0.61	<0.33	<0.83	<0.35	<0.49	0.4(3)	0.2(2)	<1.6	0.7(2)
Cr	0.53(4)	0.12(3)	0.47(5)	0.77(7)	0.76(5)	0.19(3)	0.73(3)	0.93(8)	0.79(3)
Mn	0.8(1)	0.5(1)	1.0(1)	0.6(1)	0.9(1)	0.15(6)	0.65(8)	1.1(3)	0.7(1)
Fe	0.23(2)	0.16(2)	0.40(2)	0.20(3)	0.36(3)	0.035(7)	0.39(2)	0.32(7)	0.36(2)
Co	0.2(1)	0.2(1)	<0.17	<0.34	1.0(2)	<0.31	0.6(2)	0.7(2)	0.29(7)
Ni	0.37(5)	0.26(5)	0.14(6)	0.48(9)	0.90(9)	0.13(4)	0.33(5)	0.8(1)	0.47(5)

Errors are 1σ, given as last significant digit in parentheses.
Upper limits have 2σ confidence level.

Table 3. Correlation coefficients (CC) between element ratios from crater residues and those from various chondrite types (Lodders and Fegley 1998) and Allende chondrules (Rubin and Wasson 1987).

Chondrite type	CC	Chondrite type	CC
CI	0.897	H	0.908
CM	0.901	L	0.955
CV	0.922	LL	0.966
CO	0.912	R	0.930
CK	0.926	Acapulcoites	0.939
CR	0.911	K	0.925
CH	0.741	EH	0.852
Allende chon.	0.970	EL	0.936

fragments as well as polycyclic aromatic hydrocarbons observed before sputtering cannot be connected with the impact craters.

Contamination of the Al foil with Li, Be, B, C, and O prevents a quantitative analysis of these elements by TOF-SIMS, since secondary ion signals for these elements predominately stem from the blank. Uncertainties in the blank correction are also responsible for some of the large error bars in Fig. 12, especially for elements like Na, Si, K, Sc, and V. It is presently unknown if this contamination is indigenous to the Al foil or if it results from the conditions during the impact experiments. Ar sputtering was not sufficient to remove this contamination completely.

Although variations in element ratios from crater to crater are rather large, the average composition of all analyzed samples resembles the expected element pattern remarkably well. If compared with element ratios of different chondrite types (Lodders and Fegley 1998), the TOF-SIMS data yield correlation coefficients above 0.92 for CV and CK, and below 0.92 for other carbonaceous chondrite classes (Table 3). On the other hand, for some ordinary and other chondrite classes, correlation coefficients above 0.92 were also found, mainly due to their low Fe and Ni concentrations. Except for CI, CH, and EH chondrites, correlation coefficients are above 0.9 for all chondrite classes (Table 3). The highest correlation coefficient (0.97) was observed for geometric mean values of Allende chondrules (Rubin and Wasson 1987). Considering the size of the projectiles (~40 μm), it seems to be plausible that the projectile material mainly consists of chondrules and chondrule fragments and that fine-grained matrix material is underrepresented. Some of the smaller craters might stem from monomineralic projectiles that are individual grains not

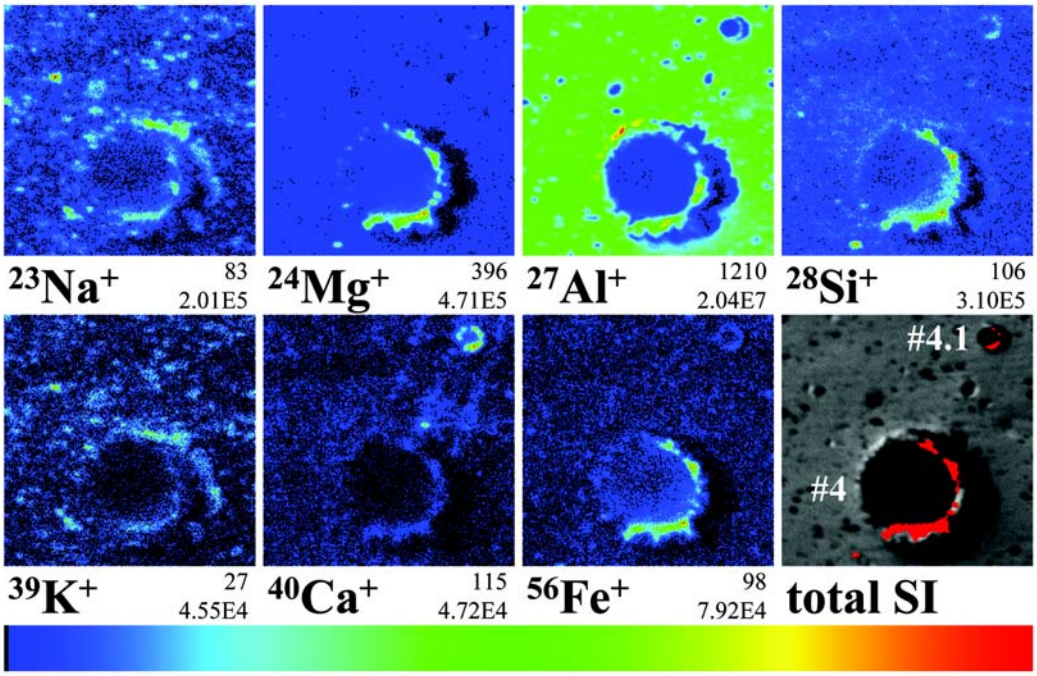

Fig. 11. TOF-SIMS secondary ion images showing two craters (UM #4 and UM #4.1) in Al foil. Field of view is 47 × 47 μm². All images use the same linear color scale normalized to the most intense pixel. Below each image, numbers for maximum and integrated intensities of the entire field of view are given. A total positive secondary ion image is given in the lower right. The apparent shadow on the right edge of both craters is attributed to the shielded area #1 in Fig. 3. Regions of interest used to calculate element ratios for both craters in Table 2 are marked in red in the total secondary ion (SI) image. For their selection the total signal from Mg, Si, Ca, and Fe was used.

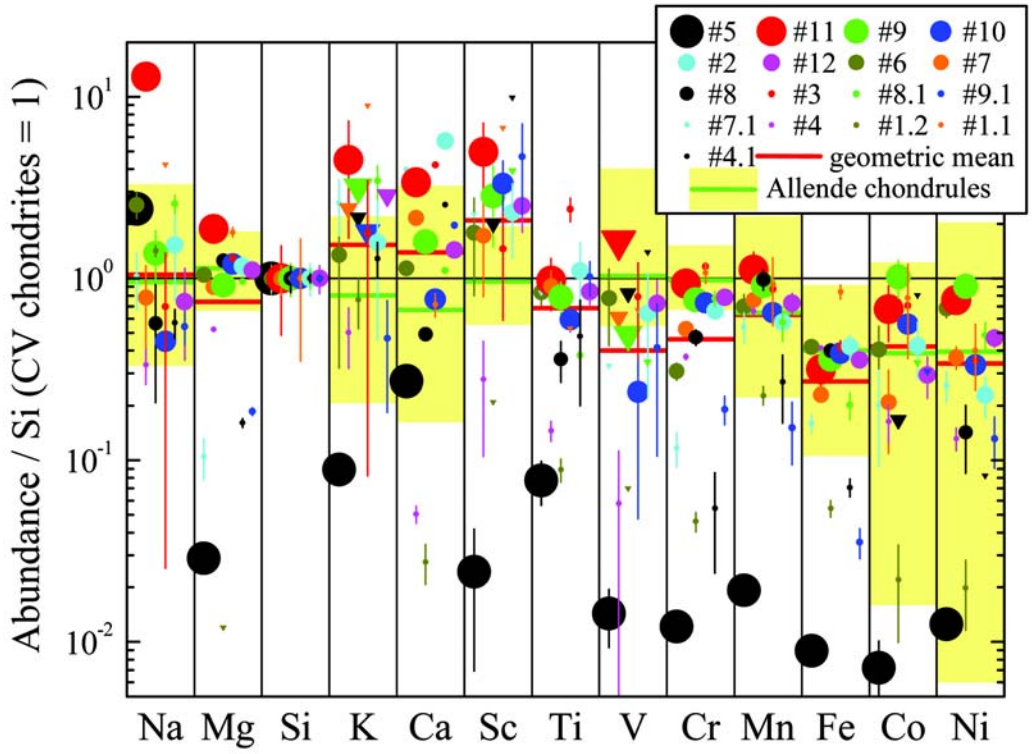

Fig. 12. Element ratios of impact residues, normalized to Si and CV chondrites, show huge variations. Symbol sizes correspond to crater dimensions. Triangles represent upper limits. Average values were calculated using all samples except UM #1.2 and #5, which are attributed to contamination. Most element ratios, especially for the large craters, are within the range defined by Allende chondrules (Rubin and Wasson 1987).

representative of Allende bulk compositions. This might explain the generally larger deviation from Allende bulk values for smaller craters than for large craters (Fig. 12). However, it should be noted that from the available data set, an unequivocal assignment to a specific chondrite class could not be made. For an unambiguous classification, data for light elements, especially C, would be crucial. It is hoped that the Stardust Al targets will be less contaminated and reliable data can be obtained for those elements.

CONCLUSIONS

The achievable lateral resolution and precision of NanoSIMS measurements of O isotopic ratios of material inside the craters, produced at the Stardust encounter speeds, is sufficient to identify presolar matter. Longer measurement times or smaller field of views would result in an even better precision than presently observed. If presolar grains are embedded in material of solar system origin, their recognition depends, of course, also on their survival during the impact into the Al foils. C-rich material in the Allende craters is mainly localized in hot spots and the achievable precision for $^{13}C/^{12}C$ ratios in 150–500 nm sized particles (several percent) would be sufficient to identify presolar matter among the Stardust material. For the N isotopes, longer measurement times appear desirable in order to decrease the counting statistical error on the $^{15}N/^{14}N$ ratio in N-bearing grains of the size considered here (150–500 nm); this, in principle, should be possible.

The TOF-SIMS results suggest that chondritic projectiles impinging on Al foils at ~6 km/sec can be identified by subsequent TOF-SIMS analysis of their residues. Despite the presence of craters with non-chondritic material, the average composition of a majority of craters is close to the chondritic composition for most major rock-forming elements. However, for a more detailed assignment of the projectile material to the specific chondrite classes, information on light elements is needed. Although uncertainties in element fractionation due to impact and crater topography cannot be completely ruled out, no obvious indication for such fractionation was found: we did not observe any systematic depletions or enrichments of volatile or refractory elements.

Acknowledgments–We thank J. Huth for his tremendous efforts to characterize the craters by SEM/EDX, E. Gröner for technical assistance on the NanoSIMS at the Max Planck Institute for Chemistry, and K. Klemm for technical assistance on the TOF-SIMS measurements. We also wish to thank A. Kearsley, D. Rost, an anonymous reviewer, and Associate Editor Ian Lyon for their critical and helpful reviews. NanoSIMS measurements in St. Louis were supported by NASA grant NNG05GJ26G.

Editorial Handling—Dr. Ian Lyon

REFERENCES

Brownlee D. E., Tsou P., Anderson J. D., Hanner M. S., Newburn R. L., Sekanina Z., Clark B. C., Hörz F., Zolensky M. E., Kissel J., McDonnell J. A. M., Sandford S. A., and Tuzzolino A. J. 2003. Stardust: Comet and interstellar dust sample return mission. *Journal of Geophysical Research*, doi:10.1029/2003JE002087.

Floss C. and Stadermann F. J. 2004. Isotopically primitive interplanetary dust particles of cometary origin: Evidence from nitrogen isotopic compositions (abstract #1281). 35th Lunar and Planetary Science Conference. CD-ROM.

Floss C., Stadermann F. J., Bradley J., Dai Z. R., Bajt S., and Graham G. 2004. Carbon and nitrogen isotopic anomalies in an anhydrous interplanetary dust particle. *Science* 303:1355–1358.

Hörz F., Bernhard R. P., and See T. H. 1995. Hypervelocity penetrations in aluminum 6061 and 1100 alloys. In *Shock-wave and high strain rate phenomena*, edited by Murr L. E., Staudhammer K. P., and Meyers M. A. Amsterdam: Elsevier Science. pp. 273–283.

Hillion F., Daigne B., Girard F., Slodzian G., and Schuhmacher M. 1994. A new high performance instrument: The Cameca "Nanosims 50." In *Secondary ion mass spectrometry: Sims IX proceedings of the Ninth International Conference on Secondary Ion Mass Spectrometry*, edited by Benninghoven A., Nihei Y., Shimizu R., and Werner H. W. Chichester: John Wiley & Sons. pp. 254–257.

Hoppe P. and Besmehn A. 2002. Evidence for extinct vanadium-49 in presolar silicon carbide grains from supernovae. *The Astrophysical Journal* 576:L69–L72.

Hoppe P. and Zinner E. 2000. Presolar dust grains from meteorites and their stellar sources. *Journal of Geophysical Research* 105: A10,371–A10,385.

Jessberger E. K. and Kissel J. 1991. Chemical properties of cometary dust and a note on carbon isotopes. In *Comets in the post-Halley era*, edited by Newburn R. L., Neugebauer M., and Rahe J. Dordrecht: Kluwer Academic Publishers. pp. 1075–1092.

Jessberger E. K., Christoforidis A., and Kissel J. 1988. Aspects of the major element composition of Halley's dust. *Nature* 332:691–695.

Kearsley A., Burchell M. J., Hörz F., Cole M. J., and Schwandt C. S. 2006. Laboratory simulation of impacts on aluminium foils of the Stardust spacecraft: Calibration of dust particle size from comet Wild-2. *Meteoritics & Planetary Science* 41. This issue.

Leroux H., Borg J., Troadec D., Djouadi Z., and Hörz F. 2006. Microstructural study of micron-sized craters simulating Stardust impacts in aluminium 1100 targets. *Meteoritics & Planetary Science* 41. This issue.

Lodders K. and Fegley B., Jr. 1998. *The planetary scientist's companion*. New York: Oxford University Press. 371 p.

Messenger S., Keller L. P., Stadermann F. J., Walker R. M., and Zinner E. 2003. Samples of stars beyond the solar system: Silicate grains in interplanetary dust. *Science* 300:105–108.

Messenger S. and Walker R. M. 1997. Evidence for molecular cloud material in meteorites and interplanetary dust. In *Astrophysical implications of the laboratory study of presolar materials*, edited by Bernatowicz T. J. and Zinner E. K. AIP Conference Proceedings #402. Woodbury, New York: American Institue of Physics. pp. 545–564.

Mostefaoui S. and Hoppe P. 2004. Discovery of abundant in situ silicate and spinel grains from red giant stars in a primitive meteorite. *The Astrophysical Journal* 613:L149–L152.

Nguyen A. N. and Zinner E. 2004. Discovery of ancient silicate stardust in a meteorite. *Science* 303:1496–1499.

Nittler L. R., Alexander C. M. O., Gao X., Walker R. M., and

Zinner E. 1997. Stellar sapphires: The properties and origins of presolar Al_2O_3 in meteorites. *The Astrophysical Journal* 483: 475–495.

Rost D., Stephan T., and Jessberger E. K. 1999. Surface analysis of stratospheric dust particles. *Meteoritics & Planetary Science* 34: 637–646.

Rubin A. E. and Wasson J. T. 1987. Chondrules, matrix and coarse-grained chondrule rims in the Allende meteorite: Origin, interrelationships and possible precursor components. *Geochimica et Cosmochimica Acta* 51:1923–1937.

Stadermann F. J., Amari S., Foote J., Swan P., Walker R. M., and Zinner E. 1994 SIMS chemical and isotopic analysis of impact features from LDEF experiment A0187-1 and A0187-2. *LDEF—69 months in space*, part 3. NASA CP #3275. pp. 461–473.

Stadermann F. J., Croat T. K., Bernatowicz T. J., Amari S., Messenger S., Walker R. M., and Zinner E. 2005. Supernova graphite in the NanoSIMS: Carbon, oxygen and titanium isotopic compositions of a spherule and its TiC sub-components. *Geochimica et Cosmochimica Acta* 69:177–188.

Stadermann F. J. and Floss C. 2004. Discovery of presolar corundum (and SiC?) in an interplanetary dust particle (abstract #9045). Workshop on Chondrites and the Protoplanetary Disk.

Stephan T. 2001. TOF-SIMS in cosmochemistry. *Planetary and Space Science* 49:859–906.

Stephan T. 2003. TOF-SIMS: A powerful tool for the analysis of stardust (abstract). Workshop on Chondrites and the Protoplanetary Disk. p. 71.

Stephan T., Stadermann F. J., Cramer H.-G., and Zehnpfenning J. 1992. TOF-SIMS analysis of LDEF impact residues (abstract). Proceedings, 23rd Lunar and Planetary Science Conference. pp. 1357–1358.

Stephan T., Jessberger E. K., and Bischoff A. 1995. Hubble Space Telescope solar array microparticulate impact analysis. In *ESTEC Workshop on Space Debris on HST, Noordwijk*. 25 p.

Stephan T., Jessberger E. K., Heiss C. H., and Rost D. 2003. TOF-SIMS analysis of polycyclic aromatic hydrocarbons in Allan Hills 84001. *Meteoritics & Planetary Science* 38:109–116.

Tsou P., Brownlee D. E., Sandford S. A., Hörz F., and Zolensky M. E. 2003. Wild 2 and interstellar sample collection and Earth return. *Journal of Geophysical Research*, doi:10.1029/2003JE002109.

Yada T., Stadermann F. J., Floss C., Zinner E., Olinger C. T., Graham G. A., Bradley J. P., Dai Z., Nakamura T., Noguchi T., and Bernas M. 2005. Discovery of abundant presolar silicates in subgroups of Antarctic micrometeorites (abstract #1227). 36th Lunar and Planetary Science Conference. CD-ROM.

Zinner E. 1989. Isotopic measurements with the ion microprobe. In *New Frontiers in stable isotope research: Laser probes, ion probes, and small-sample analysis*, edited by Shanks W. C. III and Criss R. E. USGS Bulletin 1890. pp. 145–162.

Zinner E. K. 2003. Presolar grains. In *Meteorites, comets, and planets*, edited by Davis A. M., Holland H. D., and Turekian K. K. Treatise on geochemistry, vol. 1. Oxford: Elsevier-Pergamon. pp. 17–39.

Zinner E., Nittler L. R., Hoppe P., Gallino R., Straniero O., and Alexander C. M. O'D. 2005. Oxygen, magnesium and chromium isotopic ratios of presolar spinel grains. *Geochimica et Cosmochimica Acta* 69:4149–4165.